Chapter 3

Anomalous Hall effect due to gapped nodal line in Co_2FeGe Heusler compound

This work is authored by Gaurav K. Shukla et al. and published in Phys. Rev. B 104, 195108 (2021).

In this chapter, we studied the anomalous Hall effect (AHE) in Co_2FeGe Heusler compound, which is predicted to show the intrinsic anomalous Hall conductivity (AHC) due to the gapped nodal line. We performed the experimental and theoretical study to analyze and understand the AHE in the system.

3.1 Introduction

Weyl semimetals (WSMs) host exotic transport properties resulting from their non-trivial topological band structure [1–6]. WSMs are characterized by chiral anomaly and linear band crossing points known as Weyl points or Weyl nodes [7]. The existence of Weyl nodes is possible in metal or semimetal with broken inversion symmetry (IS) and/or time-reversal symmetry (TRS). These broken symmetries lift the two-fold degeneracy of electronic bands in the framework of Kramer's theorem[8] and the linearly dispersing touching points of two non-degenerate bands become Weyl points [9, 10]. The Hamiltonian of the system describing Weyl nodes can be written in terms of the basis vector of three Pauli matrices and hence any perturbation with a linear combination of Pauli matrices can not destroy the Weyl nodes [9]. Also, no other symmetries are required (except translational symmetry) for the protection of Weyl nodes that represent the Weyl nodes as topologically stable objects [11]. Michel Berry introduced the concept of Berry curvature [12] which may be mapped to the pseudo magnetic field and the degenerate Weyl points correspond to quantized monopoles form source and sink of Berry curvature. These concepts help us to understand the various intriguing phenomena like anomalous Hall effect (AHE) [13, 14], anomalous Nernst effect (ANE) [15], chiral magnetoresistance [2, 7] and second harmonic generation [2] etc. Weyl points induced by the breaking of IS was observed experimentally first time in TaAs [16–18] and investigated extensively in its family members [19, 20] and also in other materials [21–23]. TRS-breaking WSMs are also known as magnetic WSMs discovered very recently and created much interest due to exhibiting large intrinsic AHE and anomalous Hall conductivity (AHC) which is proportional to the separation of Weyl nodes [13, 24, 25]. The magnetic WSMs have added advantage over conventional WSMs because an external magnetic field can be used to manipulate the properties of magnetic WSMs [26]. $Co_3Sn_2S_2$, a ferromagnet kagome lattice is first discovered as magnetic WSM exhibits large Berry curvature resulting in the giant intrinsic AHC 1130 S/cm, which is an or-

der of magnitude larger than the typical ferromagnets[27]. This large Berry curvature is attributed to the presence of Weyl nodes and nodal rings of linear crossings in the spin-up channel based on band inversion. Besides, $Co_3Sn_2S_2$, several other materials such as pyrochlore iridates [28–30], PrAlGe [26], $YMnBi_2$ [31], Mn_3Sn [32], $Co_3MM'X_2$ (M/M' = Ge, Sn, Pb, X=S, Se, Te) [33] and Heusler alloys [24, 34–37] have been identified as magnetic WSMs theoretically and/or experimentally.

Among various magnetic WSM candidates, Co-based Heusler compounds are more interesting that drive the large AHC due to a large Berry curvature [24, 34, 35, 38]. In most of the Co-based magnetic WSMs, a gapped nodal line in momentum space has been found as a major source of Berry curvature and creates intrinsic AHE [24, 39, 40]. In these compounds, three gapless nodal lines which are protected by three mirror planes exist in the absence of magnetization. The gapless nodal line gaps out with the introduction of spin-orbit coupling (SOC) according to the magnetization direction [13, 39]. For example, Co_2MnGa exhibits a giant AHC around 1260 S/cm at 60 K due to large Berry curvature associated with the gapped nodal line [40]. Co_2VGa exhibits the AHC around 140 S/cm due to a slightly gapped nodal line resulting from reduced mirror symmetry upon introducing magnetization [15]. Recently, Co_2MnAl Weyl semimetal was reported to have large AHC 1600 S/cm at 2 K due to a gapped nodal ring in momentum space which is as large as for 3D quantum AHE [24].

Theoretical investigation performed on the Co_2FeGe Heusler compound reveals the existence of nodal line above the Fermi energy (E_F) results in an intrinsic AHE [14, 41]. In this work, we present a study of AHE on Co_2FeGe Heusler compound using both experiment and theoretical calculations. We found the experimental AHC $\sim$ 100 S/cm at 300 K and shows weak temperature dependence. Our first-principles calculation reveals that the magnetization-induced gapped nodal line near the E_F is the main source of AHE in Co_2FeGe.

3.2 Experiment and method

Polycrystalline Co_2FeGe compound was synthesized by standard arc melting technique [42] in the presence of pure argon atmosphere using 99.99% pure individual elements. The sample was remelted several times for the homogeneous mixing of involved elements. A small weight loss

of 0.62 % was notified after melting. A small piece was taken from the sample and crushed into powder for X-ray diffraction measurement. The polished rectangular piece of the dimension $4 \times 2 \times 0.65$ mm^3 was used for temperature and magnetic field-dependent transport measurements using a cryogen-free measurement system (Cryogenic, CFMS). To obtain the actual transverse resistivity(ρ_{H}), raw Hall resistivity data ($\rho_{\mathrm{H}}{}^{raw}$) was anti-symmetrized by averaging the difference of $\rho_{\mathrm{H}}{}^{raw}$ at the positive field and negative field concerning the field sweep direction. The electronic band structure and magnetic properties of the Co_2FeGe are calculated employing density functional theory (DFT) using the Vienna-ab initio simulation package (VASP) [43]. The exchange-correlation potential is approximated with generalized gradient approximation and the projector augmented wave method (PAW)[44] is used for core-valence interaction. The calculations are performed with K-mesh of 10×10×10 for the $Fm\bar{3}m$ space group (space group no.225). The plane-wave basis is used with cut-off energy 500 eV and force convergence for the optimization is kept below 0.001 eV/Å. Self-consistent calculations are performed to get the charge density and thereafter the band structure is calculated. To understand the DFT band structure, Wannier interpolated bands and corresponding tight-binding parameters are calculated using Wannier90 [45, 46]. The anomalous Hall conductivity (AHC), Berry curvature, and energy gap for the given parameters are calculated using the WannierTool [47]. For AHC calculation Kubo formalism is used in the clean limit [48]. Co_2FeGe material possess $Fm\bar{3}m$ symmetry and have three relevant mirror planes $m_x(k_x=0)$, $m_y(k_y=0)$, $m_z(k_z=0)$ and three C_4 rotation axes k_x,k_y and k_z [35]. The magnetization is oriented along the z-axis and the SOC is also considered along the same axis.

3.3 Result and discussion

3.3.1 Structural properties

X-ray diffraction (XRD) pattern of the sample collected at room temperature for structural investigation and phase purity. The Rietveld analysis of the XRD pattern was done using Fullprof software [49]. The space group $Fm\bar{3}m$ and Wyckoff positions: 8c (1/4, 1/4, 1/4) occupied by Co atoms, whereas 4b (1/2, 1/2, 1/2) and 4a (0, 0, 0) occupied by Fe and Ge atoms, respectively were used. The observed XRD patterns depicted in Fig.3.1(a) show that all the Bragg peaks observed are well

indexed confirming the phase purity (cubic) of the Co_2FeGe sample. The refined unit cell parameter was found 5.74 Å.

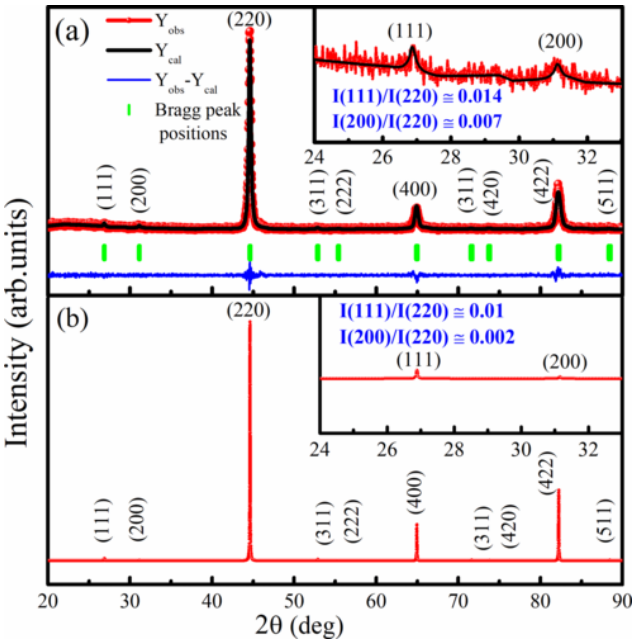

Figure 3.1: (a)Rietveld modeling of X-ray diffraction pattern of Co_2FeGe at room temperature.(b) Simulated XRD pattern of Co_2FeGe. The Inset of the figures shows the enlarged view around the (111) and (200) superlattice reflections.

For full Heusler alloys, the reflections index relation h, k and l = odd number or $(h+k+l)/2 = (2n+1)$ are the superlattice reflection, while $(h+k+l)/2 = 2n$ are the fundamental reflections[50, 51]. The ordered structure of full Heusler alloys ($L2_1$ structure) generally marks the presence of (111) and (200) superlattice reflections; the presence of (111) peak indicates the chemical ordering of atom at the octahedral position, and (200) peak indicates the ordering at the tetrahedral position, while the intensity of (220) fundamental reflection is independent of atomic ordering [52]. The presence of both (111) and (200) superlattice peaks primarily suggest the $L2_1$ structure of Co_2FeGe as shown in inset of Fig.3.1a. To compare the experimentally observed relative intensities of the superlattice reflections with theory, we simulated the XRD pattern using powder cell software as shown in Fig.3.1b. Similar to the observed, weak intensities of (111) and (200) superlattice reflections have also been observed in simulated XRD pattern. The enlarged view of simulated superlattice peaks is shown in the inset of Fig.3.1b. The weak intensity of superlattice reflections is due to the small difference between the atomic scattering factor of constituent $3d$ metals of Co_2FeGe [53, 54]. The measured and simulated $\frac{I_{111}}{I_{220}}$ and $\frac{I_{200}}{I_{220}}$ are given in inset of Fig.3.1a and Fig.3.1b respectively. A

good match between the measured and simulated XRD pattern suggests the formation of an ordered structure of Co_2FeGe.

3.3.2 Magnetization and resistivity measurements

Magnetic isotherms up to a field of 5 T were recorded at temperatures 2 K and 300 K depicted in Fig.3.2a. The magnetic moment was found to be 5.38 μ_B/f.u and 5.24 μ_B/f.u at 2 K and 300 K, respectively. The observed magnetic moment is well in agreement with the literature [55, 56] as well as our theoretical calculation (discussed later). The variation of longitudinal resistivity (ρ_{xx}) as a function of temperature from 10 K to 300 K is shown in Fig.3.2b. The ρ_{xx} increases with increasing temperature and a residual resistivity of about 14 $\mu\Omega$cm is observed. The non-linear behavior of resistivity above 50 K suggests the combined phonon and magnon scattering state [57]. The residual resistance ratio (RRR= $\rho_{xx}(300K)/\rho_{xx}(10K)$) which quantifies the degree of disorder is 2.82. This value is larger than most of Co-based Heusler alloy [39, 58–61] signifies comparatively clean sample.

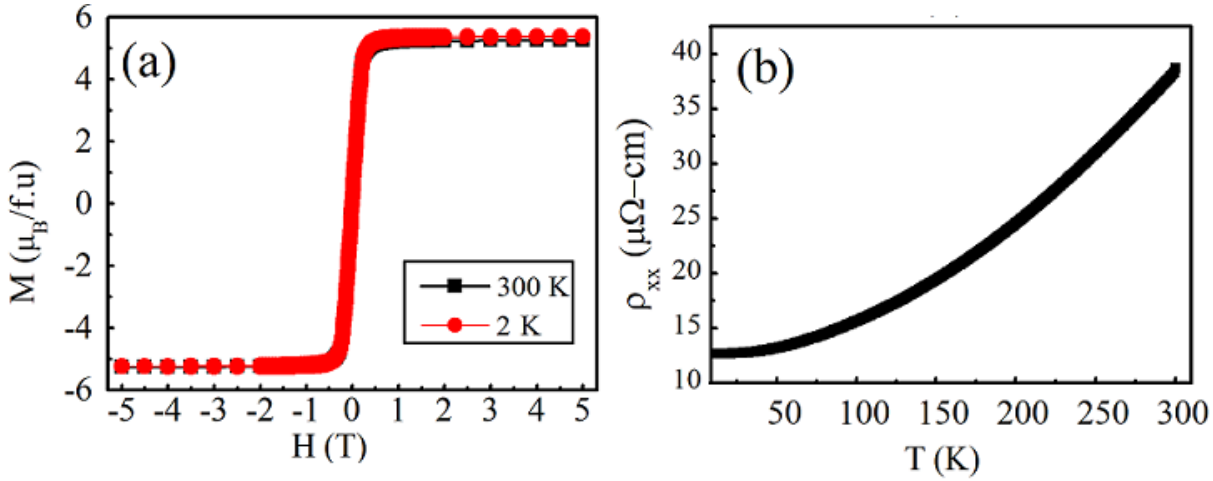

Figure 3.2: (a) The field dependent magnetization curves at 2 K and 300 K. (b) Temperature-dependent longitudinal resistivity ρ_{xx}.

3.3.3 Anomalous Hall

After investigation of the phase purity, saturation magnetization, and temperature variation of the longitudinal resistivity, we carried out a detailed magneto-transport measurement in a wide range of temperatures 50 K to 300 K to study the AHE in the Co_2FeGe Heusler alloy. Hall resistivity

(ρ_H) curves measured up to 4 Tesla magnetic field at different temperatures are shown in Fig.3.3a. The ρ_H is given by equation $\rho_H(H)$ = R_0H + R_sM [39, 62], where R_0 and R_s are the normal and anomalous Hall coefficients. H is the external applied magnetic field and M is the magnetization of the material. It is evident from Fig.3.3a that ρ_H initially increases at lower fields indicating AHE in Co_2FeGe and shows the positive slope according to sign of ordinary Hall coefficient at higher field region for all temperatures. The anomalous Hall resistivity (ρ_{AH}) calculated by the zero field extrapolation of high field Hall data with the ordinate, which is equivalent to Hall voltage response arising due to spontaneous magnetization in the absence of external magnetic field. Fig.3.3b, shows the extracted ρ_{AH} versus temperature plot, which displays that the Hall resistivity increases with increasing temperature and acquire a maximum value of 0.14$\mu\Omega$-cm at room temperature and a small value 0.02 $\mu\Omega$-cm at 50K. The slope of high field Hall resistivity data gives the normal Hall coefficient (R_0) and variation of R_0 with temperature is shown in Fig 3.3c. By using relation R_0=$\frac{1}{ne}$, we calculated carrier density (n) and plotted in the inset of Fig.3.3 (c) with temperature. The value of n was found $\sim 2\times10^{21}$/cm^3. The positive value of R_0 indicates that the holes are the majority of charge carriers in the whole temperature range. In order to investigate the origin of AHE, we analyzed the ρ_{AH} versus ρ_{xx} on a double logarithmic scale. A linear fitting was employed to determine the exponent β according to the scaling relation $\rho_{AH} \propto \rho_{xx}^{\beta}$ [61, 63] shown in Fig.3.3(d). The exponent β decides the dependency of ρ_{AH} on ρ_{xx}. According to the well-established theory of AHE, β =1 is for the AHE originates from the skew scattering mechanism and β= 2 is for the AHE governed by scattering independent mechanism [64]. By this procedure, we found the exponent $\beta = 1.75$, which indicates the Berry phase mechanism as the dominant contribution in AHE. To find the value of intrinsic AHC, we have plotted ρ_{AH} versus ρ_{xx} (Inset of Fig.3.3d) and fitted with equation

$$\rho_{AH} = a\rho_{xx} + b{\rho_{xx}}^2 \tag{3.1}$$

Here a and b are the skew scattering coefficient and intrinsic AHC, respectively. By this, we found a= 0.0004 and intrinsic AHC $b \sim 78$ S/cm. The AHC due to extrinsic side jump contribution usually the order of $e^2/ha(\epsilon_{SOC}/E_F)$, where ϵ_{SOC}, E_F and a are the spin-orbit interaction energy, Fermi energy, and lattice parameter, respectively [65]. For metallic ferromagnets ϵ_{SOC}/E_F is generally less than 10^{-2} [61, 66] and hence the side jump contribution in AHC is too small or negligible in

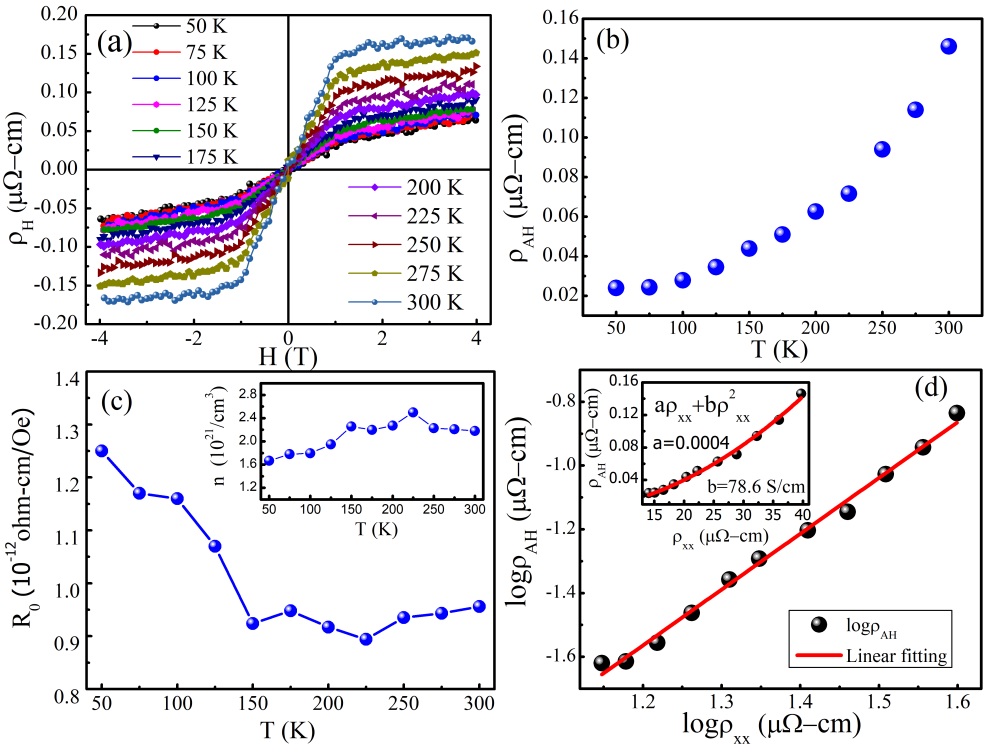

Figure 3.3: (a) Field dependent Hall resistivityρ_{H} at indicated temperatures. (b) Temperature-dependent anomalous Hall resistivity ρ_{AH}. (c) Temperature-dependent normal Hall coefficient R_0. The inset shows the temperature-dependent carrier concentration n. (d) Double logarithmic plot between ρ_{AH} and ρ_{xx} (black balls) and linear fitting is shown by red line. Inset shows the graph between ρ_{AH} and ρ_{xx} (black balls) and fitting using Eq.(3.1) is shown by the red line.

comparison to intrinsic AHC. Further, to understand the microscopic origin of AHE, we need to look towards the variation of AHC with temperature and/or longitudinal resistivity. For this, we calculated Hall conductivity using the tensor conversion formula

$$\sigma_{\mathrm{H}} = \frac{\rho_{\mathrm{H}}}{(\rho_{\mathrm{xx}}{}^2 + \rho_{\mathrm{H}}{}^2)} \tag{3.2}$$

Fig.3.4a displays the field-dependent Hall conductivity curves at indicated temperatures. The AHC was calculated by zero field extrapolation of high field Hall conductivity data on the y-axis and found close to 100 S/cm at room temperature. Fig.3.4b shows the variation of longitudinal conductivity and AHC with temperature. AHC is nearly insensitive to temperature from several K to 300K, while the longitudinal resistivity shows explicit temperature dependence, fairly indicating the origin of AHE governed by the intrinsic mechanism [63, 67, 68]. Since the intrinsic AHE merely depends on the band structure of the material. Therefore to get a better understanding of the origin of intrinsic AHE, we carried out the first principles calculation on Co_2FeGe .

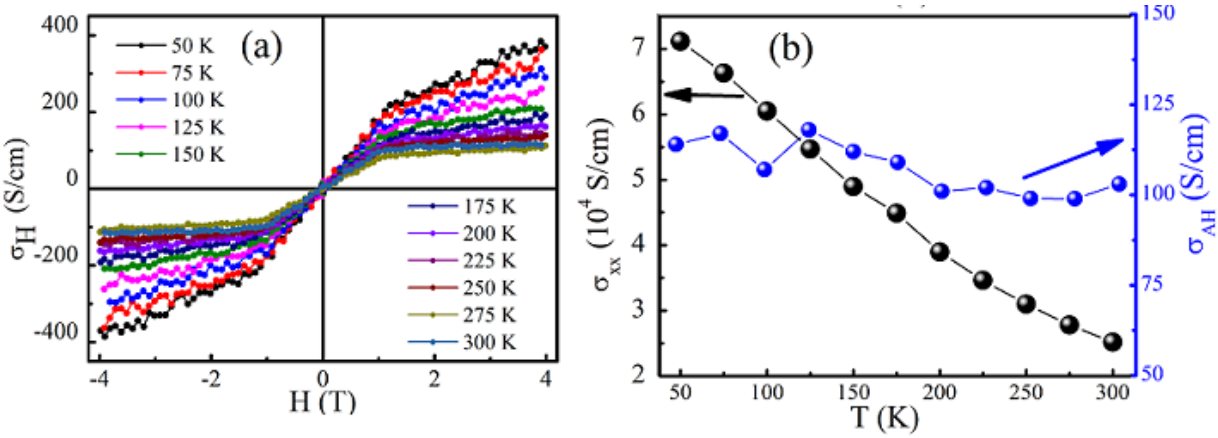

Figure 3.4: (a) Field dependent Hall conductivity σ_{H} (b) Temperature dependent longitudinal conductivity σ_{xx}(black spheres) and AHC (blue spheres).

3.3.4 Theoretical calculations

Our ab initio calculation for a magnetic moment suggests that Fe and Co have a large magnetic moment with μ_{Fe}=2.84 μ_B/f.u and μ_{Co}=1.34 μ_B/f.u respectively, whereas Ge has a small vanishing magnetic moment. The total magnetic moment per formula unit is 5.53 μ_B, aligned along the (001) direction and the d-orbital of the transition atoms Fe and Co are the major contributors. The magnetic moment of full Heusler alloys generally follows the Slater Pauling (SP) rule[69]; $M = Z-24$, where M and Z are magnetic moments and the number of valance electrons if the E_F lies in the band gap of the minority spin states. For Co_2FeGe, as per SP rule the total magnetic moment should be 6 μ_B/f.u. In some cases these systems may have gapless minority bands or minority bands crossing the E_F, then a small deviation in total magnetic moment from the SP rule may be expected [69]. The calculated magnetic moment for Co_2FeGe is in agreement with the experimental value (5.38 μ_B/f.u), but this value is smaller than predicted by the SP rule. To understand the deviation of magnetic moment total density of state (DOS) is calculated and shown in Fig.3.5a. Total DOS of minority spin electrons have finite value at E_F, which indicates the presence of gapless states at the E_F or bands crossing E_F. A similar finite value of total DOS at E_F is also reported in the literature for onsite Coulomb interaction $U = 0$ [55, 70, 71]. We also performed calculations considering onsite Coulomb repulsion U; 1.92 and 1.8 for the Co and Fe, respectively [72] and the calculated value of the magnetic moment is ≈ 6.00 μ_B/f.u, which overestimates relative to experimental value, however, the magnetic moment is in agreement with literature [54, 55, 71]. Therefore, we believe

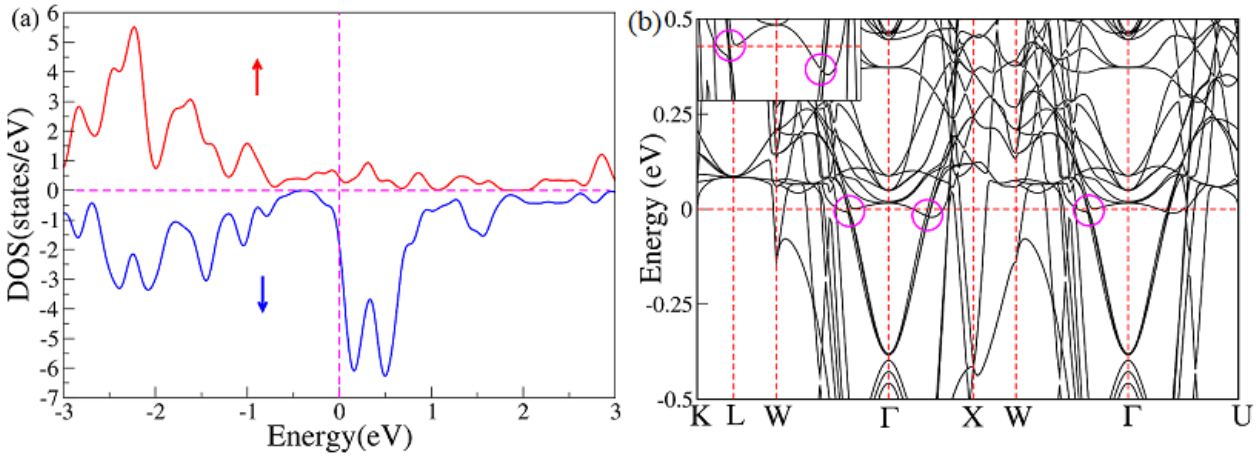

Figure 3.5: (a) The total density of state (DOS) of Co_2FeGe for on site Coulomb interaction U=0. Red and blue curves represent the total DOS for majority and minority spins. (b)The band structure of Co_2FeGe in the presence of SOC (gapped nodal lines are shown in a circle and the inset shows the enlarged view around the gapped nodal line).

that $U = 0$ is a more suitable parameter to explain the experimental findings. A similar conclusion is also reported for other Co-based Heusler alloys [35, 73]. This material is expected to show nodal line due to three relevant mirror planes $m_x(k_x$=0), $m_y(k_y$=0), $m_z(k_z$=0) in absence of SOC [41]. In the presence of SOC, the nodal lines will gap out according to the magnetization direction and introduce Berry curvature in the system [13, 41]. To understand the topological aspects, the nodal lines in the electronic band structure are analyzed in the absence and presence of SOC. The band structure with SOC coupling is calculated from the DFT calculation shown in Fig.3.5b. The band crossings are gaped out just below or at the E_F due to the perturbation of SOC and these tiny gaps are shown inside the circle.

We analyzed the spectrum of the tight-binding model Hamiltonian calculated from the Wannier90 [45, 46] calculation with the help of Wanniertool [47]. In Fig.3.6a and Fig.3.6b, we have shown the energy gap between the lowest conduction band and the topmost valence band at k_x=0 plane, and gaps are shown on a logarithmic scale of color plot in absence as well as in the presence of SOC, respectively. The gaps smaller than 10^{-4} eV are considered to be gapless. We noticed that four semi-circular nodal lines appear in $k_y - k_z$ plane of the first Brillouin zone (Fig.3.6a) and in the presence of the SOC, the gapless semi-circular nodal lines are gaped out (Fig.3.6b). This material shows an intrinsic AHC, which can be expressed within the framework of linear response theory of the Kubo formalism[48];

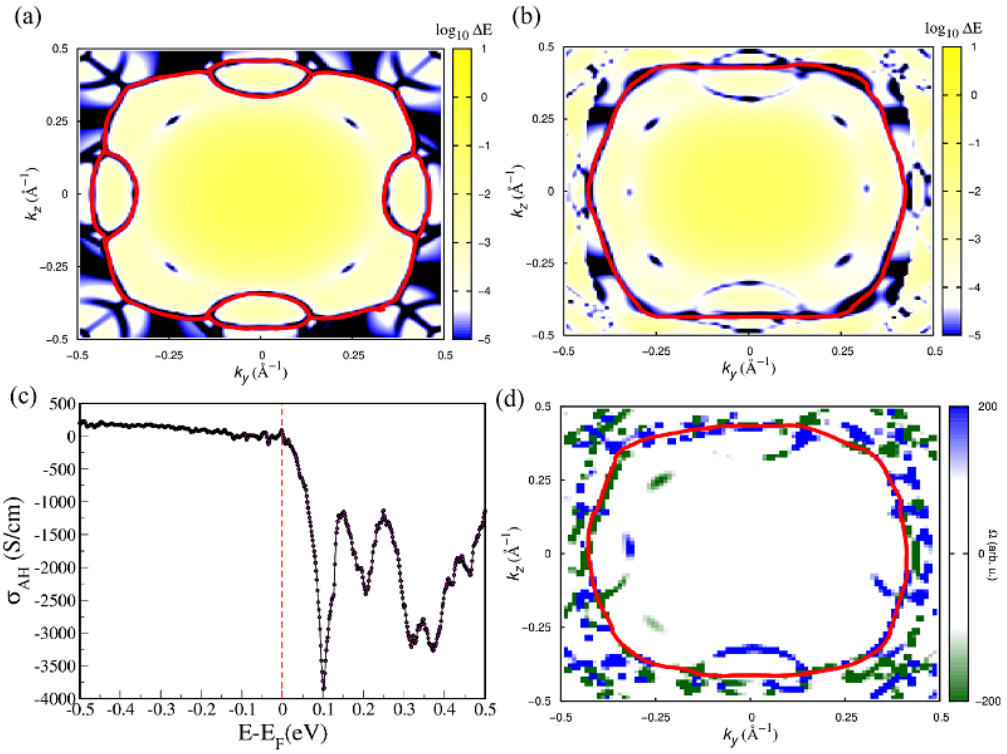

Figure 3.6: Energy gap $\Delta E(k_y, k_z)$ is plotted in k_y-k_z plane at $k_x = 0$ (a) without SOC (b) with SOC. Solid red lines represent gapless regions. (c) Energy ($E - E_F$) dependence of the AHC. (d) Berry curvature distribution in k_y-k_z plane at $k_x = 0$.Solid red lines represent gapless regions.

$$\sigma_{\alpha\beta} = -\frac{e^2}{\hbar}\sum_n \int \frac{d^3k}{(2\pi)^3}\Omega^n_{\alpha\beta}(k) f_n(k) \tag{3.3}$$

where Berry curvature Ω can be written as a sum over eigenstates[74].

$$\Omega^n_{\alpha\beta} = i\sum_{n\neq n'} \frac{\langle n|\frac{\partial H}{\partial R^\alpha}|n'\rangle\langle n'|\frac{\partial H}{\partial R^\beta}|n\rangle - (\alpha \leftrightarrow \beta)}{(\epsilon_n - \epsilon_{n'})^2} \tag{3.4}$$

Here $|n\rangle$,ϵ_n and $\epsilon_{n'}$ are the energy eigenstate and eigenvalue of n and n' bands respectively. H, f_n and $\Omega^n_{\alpha\beta}$ are the Hamiltonian, Fermi distribution function, and Berry curvature respectively. The $\Omega^n_{\alpha\beta}$ is related to the change of electronic wave function within the Brillouin zone.

In Fig.3.6d, local Berry curvature is shown in $k_x = 0$ plane of the Brillouin zone. Due to the broken time-reversal symmetry and spin-orbit coupling (SOC), the mirror symmetries disrupt, resulting in an asymmetric Berry curvature in the k_x=0 plane. Intrinsic AHC is calculated using maximally localized Wannier orbitals using 101 × 101 × 101 k-grid. The intrinsic AHC is proportional to the Brillouin zone summation of the Berry curvature over all occupied states and can be calculated using

Eq.3.3. We notice that the major contribution of AHC comes from the neighborhood of nodal lines. The AHC as a function of $E - E_F$ is shown in Fig.3.6c. The calculated AHC value at E_F is found 77.29 S/cm, which well matches with the experimentally found intrinsic AHC of 78.6 S/cm. We have also calculated the energy-dependent AHC as shown in Fig.3.6c and it is evident that Fermi level shift in Co_2FeGe will result in an increased AHC.

3.4 Conclusion

In conclusion, we have experimentally investigated the AHE in Co_2FeGe Heusler alloy and performed first principle calculations to understand the origin of intrinsic AHE. Experimentally AHC was found close to 100 S/cm at 300 K with an intrinsic contribution of 78.6 S/cm. Berry curvature calculations give AHC about 77.29 S/cm due to magnetization-induced gapped nodal line near the E_F, which is in good agreement with the experimentally calculated intrinsic AHC.

References

[1] S. Wang, B.-C. Lin, A.-Q. Wang, D.-P. Yu, and Z.-M. Liao, Quantum transport in Dirac and Weyl semimetals: A review, Adv. Phys.: X **2**, 518 (2017).

[2] N. Nagaosa, T. Morimoto, and Y. Tokura, Transport, magnetic and optical properties of Weyl materials, Nat. Rev.Mater. **5**, 621 (2020).

[3] B. Yan and C. Felser, Topological materials: Weyl semimetals, Annu. Rev. Condens. Matter Phys. **8**, 337 (2017).

[4] D. Hsieh, Y. Xia, L. Wray, D. Qian, A. Pal, J. Dil, J. Osterwalder, F. Meier, G. Bihlmayer, C. Kane, *et al.*, Observation of unconventional quantum spin textures in topological insulators, Science **323**, 919 (2009).

[5] J.-L. Xu, Y.-J. Sun, J.-L. He, Y. Wang, Z.-J. Zhu, Z.-Y. You, J.-F. Li, M. M. Chou, C.-K. Lee, and C.-Y. Tu, Ultrasensitive nonlinear absorption response of large-size topological insulator and application in low-threshold bulk pulsed lasers, Sci. Rep. **5**, 14586 (2015).

[6] P. Hosur and X. Qi, Recent developments in transport phenomena in Weyl semimetals, C. R. Phys. **14**, 857 (2013).

[7] B. Lv, T. Qian, and H. Ding, Experimental perspective on three-dimensional topological semimetals, Rev. Mod. Phys. **93**, 025002 (2021).

[8] M. J. Klein, On a degeneracy theorem of kramers, Am. J. Phys. **20**, 65 (1952).

[9] T. Chen, T. Tomita, S. Minami, M. Fu, T. Koretsune, M. Kitatani, I. Muhammad, D. Nishio-Hamane, R. Ishii, F. Ishii, *et al.*, Anomalous transport due to Weyl fermions in the chiral antiferromagnets Mn_3X, (X= Sn, Ge), Nat. Commun. **12**, 572 (2021).

[10] A. Burkov, Topological semimetals, Nat. Mater. **15**, 1145 (2016).

[11] S. A. Yang, Dirac and Weyl materials: fundamental aspects and some spintronics applications, in *Spin*, Vol. 6 (World Scientific, 2016) p. 1640003.

[12] M. V. Berry, Quantal phase factors accompanying adiabatic changes, Proc. R. Soc. A: Math. Phys. Sci. **392**, 45 (1984).

[13] K. Manna, Y. Sun, L. Muechler, J. Kübler, and C. Felser, Heusler, Weyl and Berry, Nat. Rev. Mater. **3**, 244 (2018).

[14] J. Noky, J. Gooth, C. Felser, and Y. Sun, Characterization of topological band structures away from the Fermi level by the anomalous Nernst effect, Phys. Rev. B. **98**, 241106 (2018).

[15] K. Manna, L. Muechler, T.-H. Kao, R. Stinshoff, Y. Zhang, J. Gooth, N. Kumar, G. Kreiner, K. Koepernik, R. Car, *et al.*, From colossal to zero: controlling the anomalous Hall effect in magnetic Heusler compounds via Heusler curvature design, Phys. Rev. X **8**, 041045 (2018).

[16] S.-Y. Xu, I. Belopolski, N. Alidoust, M. Neupane, G. Bian, C. Zhang, R. Sankar, G. Chang, Z. Yuan, C.-C. Lee, *et al.*, Discovery of a Weyl fermion semimetal and topological Fermi arcs, Science **349**, 613 (2015).

[17] L. Yang, Z. Liu, Y. Sun, H. Peng, H. Yang, T. Zhang, B. Zhou, Y. Zhang, Y. Guo, M. Rahn, *et al.*, Weyl semimetal phase in the non-centrosymmetric compound TaAs, Nat. Phys. **11**, 728 (2015).

[18] B. Lv, N. Xu, H. Weng, J. Ma, P. Richard, X. Huang, L. Zhao, G. Chen, C. Matt, F. Bisti, *et al.*, Observation of Weyl nodes in TaAs, Nat. Phys. **11**, 724 (2015).

[19] Y. Sun, Y. Zhang, C. Felser, and B. Yan, Strong intrinsic spin Hall effect in the TaAs family of Weyl semimetals, Phys. Rev. Lett. **117**, 146403 (2016).

[20] S.-Y. Xu, I. Belopolski, D. S. Sanchez, C. Zhang, G. Chang, C. Guo, G. Bian, Z. Yuan, H. Lu, T.-R. Chang, *et al.*, Experimental discovery of a topological Weyl semimetal state in TaP, Sci. Adv. **1**, e1501092 (2015).

[21] A. A. Soluyanov, D. Gresch, Z. Wang, Q. Wu, M. Troyer, X. Dai, and B. A. Bernevig, Type-II Weyl semimetals, Nat. **527**, 495 (2015).

[22] Y. Sun, S.-C. Wu, M. N. Ali, C. Felser, and B. Yan, Prediction of Weyl semimetal in orthorhombic $MoTe_2$, Phys. Rev. B **92**, 161107 (2015).

[23] J. Liu and D. Vanderbilt, Weyl semimetals from noncentrosymmetric topological insulators, Phys. Rev. B **90**, 155316 (2014).

[24] P. Li, J. Koo, W. Ning, J. Li, L. Miao, L. Min, Y. Zhu, Y. Wang, N. Alem, C.-X. Liu, *et al.*, Giant room temperature anomalous Hall effect and tunable topology in a ferromagnetic topological semimetal Co_2MnAl, Nat. Commun. **11**, 3476 (2020).

[25] A. Zyuzin, S. Wu, and A. Burkov, Weyl semimetal with broken time reversal and inversion symmetries, Phys. Rev. B **85**, 165110 (2012).

[26] D. Destraz, L. Das, S. S. Tsirkin, Y. Xu, T. Neupert, J. Chang, A. Schilling, A. G. Grushin, J. Kohlbrecher, L. Keller, *et al.*, Magnetism and anomalous transport in the Weyl semimetal PrAlGe: possible route to axial gauge fields, npj Quantum Mater. **5**, 5 (2020).

[27] E. Liu, Y. Sun, N. Kumar, L. Muechler, A. Sun, L. Jiao, S.-Y. Yang, D. Liu, A. Liang, Q. Xu, *et al.*, Giant anomalous Hall effect in a ferromagnetic kagome-lattice semimetal, Nat. Phys. **14**, 1125 (2018).

[28] X. Wan, A. M. Turner, A. Vishwanath, and S. Y. Savrasov, Topological semimetal and Fermi

arc surface states in the electronic structure of pyrochlore iridates, Phys. Rev. B **83**, 205101 (2011).

[29] K. Ueda, R. Kaneko, H. Ishizuka, J. Fujioka, N. Nagaosa, and Y. Tokura, Spontaneous Hall effect in the Weyl semimetal candidate of all-in all-out pyrochlore iridate, Nat. Commun. **9**, 3032 (2018).

[30] K. S. Takahashi, H. Ishizuka, T. Murata, Q. Y. Wang, Y. Tokura, N. Nagaosa, and M. Kawasaki, Anomalous Hall effect derived from multiple Weyl nodes in high-mobility $EuTiO_3$ films, Sci. Adv. **4**, eaar7880 (2018).

[31] S. Borisenko, D. Evtushinsky, Q. Gibson, A. Yaresko, K. Koepernik, T. Kim, M. Ali, J. van den Brink, M. Hoesch, A. Fedorov, *et al.*, Time-reversal symmetry breaking type-II Weyl state in $YbMnBi_2$, Nat. Commun. **10**, 3424 (2019).

[32] K. Kuroda, T. Tomita, M.-T. Suzuki, C. Bareille, A. Nugroho, P. Goswami, M. Ochi, M. Ikhlas, M. Nakayama, S. Akebi, *et al.*, Evidence for magnetic Weyl fermions in a correlated metal, Nat. Mater. **16**, 1090 (2017).

[33] W. Luo, Y. Nakamura, J. Park, and M. Yoon, Cobalt-based magnetic Weyl semimetals with high-thermodynamic stabilities, npj Computational Mater. **7**, 2 (2021).

[34] I. Belopolski, K. Manna, D. S. Sanchez, G. Chang, B. Ernst, J. Yin, S. S. Zhang, T. Cochran, N. Shumiya, H. Zheng, *et al.*, Discovery of topological Weyl fermion lines and drumhead surface states in a room temperature magnet, Science **365**, 1278 (2019).

[35] G. Chang, S.-Y. Xu, H. Zheng, B. Singh, C.-H. Hsu, G. Bian, N. Alidoust, I. Belopolski, D. S. Sanchez, S. Zhang, *et al.*, Room-temperature magnetic topological Weyl fermion and nodal line semimetal states in half-metallic Heusler Co_2TiX (X=Si, Ge, or Sn), Sci. Rep. **6**, 38839 (2016).

[36] M. Hirschberger, S. Kushwaha, Z. Wang, Q. Gibson, S. Liang, C. A. Belvin, B. A. Bernevig, R. J. Cava, and N. P. Ong, The chiral anomaly and thermopower of Weyl fermions in the half-Heusler GdPtBi, Nat. Mater. **15**, 1161 (2016).

[37] W. Shi, L. Muechler, K. Manna, Y. Zhang, K. Koepernik, R. Car, J. Van Den Brink, C. Felser,

and Y. Sun, Prediction of a magnetic Weyl semimetal without spin-orbit coupling and strong anomalous Hall effect in the Heusler compensated ferrimagnet Ti_2MnAl, Phys. Rev. B **97**, 060406 (2018).

[38] R. P. Dulal, B. R. Dahal, A. Forbes, N. Bhattarai, I. L. Pegg, and J. Philip, Weak localization and small anomalous Hall conductivity in ferromagnetic Weyl semimetal Co_2TiGe, Sci. Rep. **9**, 3342 (2019).

[39] B. Ernst, R. Sahoo, Y. Sun, J. Nayak, L. Muechler, A. K. Nayak, N. Kumar, J. Gayles, A. Markou, G. H. Fecher, *et al.*, Anomalous Hall effect and the role of Berry curvature in Co_2TiSn Heusler films, Phys. Rev. B **100**, 054445 (2019).

[40] S. N. Guin, K. Manna, J. Noky, S. J. Watzman, C. Fu, N. Kumar, W. Schnelle, C. Shekhar, Y. Sun, J. Gooth, *et al.*, Anomalous Nernst effect beyond the magnetization scaling relation in the ferromagnetic Heusler compound Co_2MnGa, NPG Asia Mater. **11**, 16 (2019).

[41] J. Noky, Y. Zhang, J. Gooth, C. Felser, and Y. Sun, Giant anomalous Hall and Nernst effect in magnetic cubic Heusler compounds, npj Computational Mater. **6**, 77 (2020).

[42] D.-C. Tsai and C.-H. Chiang, Vacuum arc melting processes for biomedical NiTi shape memory alloy, in *MATEC Web of Conferences*, Vol. 30 (EDP Sciences, 2015) p. 01004.

[43] J. Hafner, Ab-initio simulations of materials using VASP: Density-functional theory and beyond, J. Comput. Chem. **29**, 2044 (2008).

[44] P. E. Blöchl, Projector augmented-wave method, Phys. Rev. B **50**, 17953 (1994).

[45] G. Pizzi, V. Vitale, R. Arita, S. Blügel, F. Freimuth, G. Géranton, M. Gibertini, D. Gresch, C. Johnson, T. Koretsune, J. Ibañez-Azpiroz, H. Lee, J.-M. Lihm, D. Marchand, A. Marrazzo, Y. Mokrousov, J. I. Mustafa, Y. Nohara, Y. Nomura, L. Paulatto, S. Poncé, T. Ponweiser, J. Qiao, F. Thöle, S. S. Tsirkin, M. Wierzbowska, N. Marzari, D. Vanderbilt, I. Souza, A. A. Mostofi, and J. R. Yates, Wannier90 as a community code: New features and applications, J. Comput. Chem. **32**, 165902 (2020).

[46] N. Marzari and D. Vanderbilt, Maximally localized generalized Wannier functions for composite energy bands,}Phys. Rev. B **56**, 12847 (1997).

[47] Q. Wu, S. Zhang, H.-F. Song, M. Troyer, and A. A. Soluyanov, Wanniertools: An open-source software package for novel topological materials, Comput. Phys. Commun. **224**, 405 (2018).

[48] M. Gradhand, D. Fedorov, F. Pientka, P. Zahn, I. Mertig, and B. Györffy, First-principle calculations of the Berry curvature of Bloch states for charge and spin transport of electrons, J. Phys. Condens. **24**, 213202 (2012).

[49] J. Rodríguez-Carvajal, An introduction to the program fullprof, Laboratoire Leon Brillouin (CEA-CNRS) (2001).

[50] Y. Takamura, R. Nakane, and S. Sugahara, Analysis of $L2_1$ ordering in full Heusler Co_2FeSi alloy thin films formed by rapid thermal annealing, J. Appl. Phys. **105**, 07B109 (2009).

[51] Y. Sakuraba, K. Hyodo, A. Sakuma, and S. Mitani, Giant anomalous Nernst effect in the $Co_2MnAl_{1-x}Si_x$ Heusler alloy induced by Fermi level tuning and atomic ordering, Phys. Rev. B **101**, 134407 (2020).

[52] S. Wurmehl, G. H. Fecher, H. C. Kandpal, V. Ksenofontov, C. Felser, and H.-J. Lin, Investigation of Co_2FeSi, the Heusler compound with highest Curie temperature and magnetic moment, Appl. Phys. Lett. **88**, 032503 (2006).

[53] B. Balke, S. Wurmehl, G. H. Fecher, C. Felser, M. d. C. M. Alves, F. Bernardi, and J. Morais, Structural characterization of the Co_2FeZ(Z= Al, Si, Ga, and Ge) Heusler compounds by X-ray diffraction and extended X-ray absorption fine structure spectroscopy, Appl. Phys. Lett. New York. Vol. 90, no. 17 (Apr. 2007), 172501, 3 p. (2007).

[54] B. Balke, S. Wurmehl, G. H. Fecher, C. Felser, and J. Kübler, Rational design of new materials for spintronics: Co_2FeZ (Z= Al, Ga, Si, Ge), Sci. Technol. Adv. Mater. (2008).

[55] D. Rai, A. Shankar, M. Ghimire, R. Thapa, *et al.*, A comparative study of a Heusler alloy Co_2FeGe using lsda and lsda+ u, Phys. B: Condens. Matter **407**, 3689 (2012).

[56] S. Amari, F. Dahmane, S. B. Omran, B. Doumi, I. Yahiaoui, A. Tadjer, and R. Khenata, Theoretical investigation of the structural, magnetic and band structure characteristics of $Co_2FeGe_{1-x}Si_x$ (x= 0, 0.5, 1) full-Heusler alloys, J. Korean Phys. Soc. **69**, 1462 (2016).

[57] D. Goodings, Electrical resistivity of ferromagnetic metals at low temperatures, Phys. Rev. **132**, 542 (1963).

[58] A. Markou, D. Kriegner, J. Gayles, L. Zhang, Y.-C. Chen, B. Ernst, Y.-H. Lai, W. Schnelle, Y.-H. Chu, Y. Sun, *et al.*, Thickness dependence of the anomalous Hall effect in thin films of the topological semimetal Co_2MnGa, Phys. Rev. B **100**, 054422 (2019).

[59] I.-M. Imort, P. Thomas, G. Reiss, and A. Thomas, Anomalous Hall effect in the Co-based Heusler compounds Co_2FeSi and Co_2FeAl, J. Appl. Phys. **111**, 07D313 (2012).

[60] E. V. Vidal, H. Schneider, and G. Jakob, Influence of disorder on anomalous Hall effect for Heusler compounds, Phys. Rev. B **83**, 174410 (2011).

[61] S. Roy, R. Singha, A. Ghosh, A. Pariari, and P. Mandal, Anomalous Hall effect in the half-metallic Heusler compound Co_2TiX (X = Si,Ge), Phys. Rev. B **102**, 085147 (2020).

[62] N. Nagaosa, Anomalous Hall effect-A new perspective, J. Phys. Soc. Jpn. **75**, 042001 (2006).

[63] Q. Wang, Y. Xu, R. Lou, Z. Liu, M. Li, Y. Huang, D. Shen, H. Weng, S. Wang, and H. Lei, Large intrinsic anomalous Hall effect in half-metallic ferromagnet $Co_3Sn_2S_2$ with magnetic Weyl fermions, Nat. Commun. **9**, 3681 (2018).

[64] N. Nagaosa, J. Sinova, S. Onoda, A. H. MacDonald, and N. P. Ong, Anomalous Hall effect, Rev. Mod. Phys. **82**, 1539 (2010).

[65] I. Campbell and A. Fert, Transport properties of ferromagnets, Handbook of Ferromagnetic Materials **3**, 747 (1982).

[66] Y. Liu, H. Tan, Z. Hu, B. Yan, C. Petrovic, *et al.*, Anomalous Hall effect in the weak-itinerant ferrimagnet $FeCr_2Te_4$, Phys. Rev. B **103**, 045106 (2021).

[67] D. Liu, A. Liang, E. Liu, Q. Xu, Y. Li, C. Chen, D. Pei, W. Shi, S. Mo, P. Dudin, *et al.*, Magnetic Weyl semimetal phase in a kagome crystal, Science **365**, 1282 (2019).

[68] X. Chen, M. Wang, C. Gu, S. Wang, Y. Zhou, C. An, Y. Zhou, B. Zhang, C. Chen, Y. Yuan, *et al.*, Pressure-tunable large anomalous Hall effect of the ferromagnetic kagome-lattice Weyl semimetal $Co_3Sn_2S_2$, Phys. Rev. B **100**, 165145 (2019).

[69] S. V. Faleev, Y. Ferrante, J. Jeong, M. G. Samant, B. Jones, and S. S. Parkin, Unified explanation of chemical ordering, the slater-pauling rule, and half-metallicity in full Heusler compounds, Phys. Rev. B **95**, 045140 (2017).

[70] K. R. Kumar, K. K. Bharathi, J. A. Chelvane, S. Venkatesh, G. Markandeyulu, and N. Harishkumar, First-principles calculation and experimental investigations on full Heusler alloy Co_2FeGe, IEEE Trans. Magn. **45**, 3997 (2009).

[71] J.-M. Hyun and M. Kim, The half-metallicity of Co_2FeGe full Heusler alloy in (001) thin film:first principles study, J. Korean Phys. Soc. **72**, 276 (2018).

[72] K. Nawa and Y. Miura, Exploring half-metallic Co-based full Heusler alloys using a DFT + U method combined with linear response approach, RSC Adv. **9**, 30462 (2019).

[73] G. Chang, S.-Y. Xu, X. Zhou, S.-M. Huang, B. Singh, B. Wang, I. Belopolski, J. Yin, S. Zhang, A. Bansil, *et al.*, Topological hopf and chain link semimetal states and their application to Co_2MnGa, Phys. Rev. Lett. **119**, 156401 (2017).

[74] D. Xiao, M.-C. Chang, and Q. Niu, Berry phase effects on electronic properties, Rev. Mod. Phys. **82**, 1959 (2010).